ACS APPLIED ELECTRONIC MATERIALS

Open Access

This article is licensed under CC-BY 4.0

pubs.acs.org/acsaelm

Article

Strain Control of (001)-Polar-Axis-Oriented Epitaxial Y-Doped HfO_2 Thin Films

Yoshiki Maekawa, Koji Hirai, Kazuki Okamoto,* Takao Shimizu, and Hiroshi Funakubo*

Cite This: *ACS Appl. Electron. Mater.* 2024, 6, 5525−5535

Read Online

ACCESS | Metrics & More | Article Recommendations | Supporting Information

ABSTRACT: {100}-Oriented epitaxial orthorhombic $(Hf_{0.93}Y_{0.07})O_2$ (7YHO) films were grown at 700 °C on various substrates, with and without $(Ce_{0.35}Zr_{0.65})O_2$ (CZO) buffer layers, by using pulsed laser deposition. The crystal phase and orientation were determined by X-ray diffraction. The long axis [100] or short axis [010]/[001] orientations were controlled by lattice matching. Nearly relaxed epitaxial orthorhombic (100) 7YHO films on $LaAlO_3$ and $SrRuO_3/SrTiO_3$ substrates were obtained, and their unclamped lattice constants were experimentally observed. The in-plane lattice parameter of the (010)/(001)-oriented 7YHO films obtained by using the CZO buffer layers was within the range of 0.518−0.523 nm. This study demonstrates selective growth and lattice strain control with respect to the in-plane lattice spacing of the underlying layers. These findings provide further possibilities for understanding the fundamental ferroelectric properties of HfO_2-based materials.

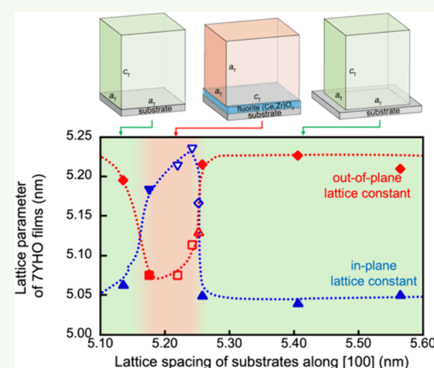

KEYWORDS: *Ferroelectric HfO_2-based film, Epitaxial film, {100} Orientation control, Polar axis orientation, Pulse laser deposition*

INTRODUCTION

The ferroelectricity of HfO_2-based materials was first reported in 2011.[1] Since then, HfO_2-based thin films have been widely and intensively investigated for ferroelectric memory applications, such as ferroelectric random access memories,[1,2] ferroelectric field-effect transistors,[3] and ferroelectric tunnel junctions.[4] These films show stable ferroelectricity even in polycrystalline thin films with thicknesses as low as 5 nm,[4,5] unlike conventional ferroelectric materials such as perovskite-structured ferroelectric films, including $Pb(Zr,Ti)O_3$ and $BaTiO_3$.[6,7]

Prompt research is required to understand the fundamental ferroelectric properties of epitaxial HfO_2-based films, such as the spontaneous polarization (P_s), Curie temperature (T_c), and orientation-dependence or strain-dependence of the ferroelectricity and piezoelectricity.[8−13] Choi et al. demonstrated that applying a large compressive strain to $BaTiO_3$ (001) films, as a conventional ferroelectric, enhances the spontaneous polarization and increases the T_c through selective growth of polar-axis-oriented films on $(001)_{pc}$ $DyScO_3$ and $(001)_{pc}$ $GdScO_3$ single-crystal substrates.[14] The selective growth of polar-axis (001)-oriented HfO_2 films is not simple due to the small crystal-anisotropy. Therefore, characterization studies generally employ (111)-oriented films on (111)ITO//(111) yttrium-stabilized zirconia (YSZ)[15] and (100)(La,Sr)MnO_3//(100)-$SrTiO_3$[16,17] substrates because the possible contribution to polarization along the surface normal direction in the films is nearly the same regardless of the type of domains formed in the films. There are several reports on {100}-oriented epitaxial films on (100)YSZ,[18] (100)Si,[19] and (100)Nb:$SrTiO_3$.[20] However, controlling the orientation of {100}-oriented films and their strain effects is not well understood.

In this study, we demonstrate control of the (100) and (010)/(001) orientation for epitaxial $(Hf_{0.93}Y_{0.07})O_2$ (7YHO) orthorhombic films by selecting an underlying layer with a lattice match. Using this approach, (100)- and (010)/(001)-oriented films with different in-plane strains are successfully grown.

DETERMINATION OF FILM ORIENTATION

The orthorhombic phase has three axes: a relatively long axis (a_O-axis) and two relatively short axes (b_O- and c_O-axes), where the subscript *o* denotes the ferroelectric orthorhombic phase. Here, the polar c_O-axis is slightly longer than the b_O-axis, but the length is roughly similar ($c_O/b_O \approx 1.004$; based on the calculated data for ferroelectric orthorhombic HfO_2 ($Pca2_1$)).[21] Herein, the a_O-axis is defined as the *long axis*, whereas the b_O- and c_O-axes are denoted as the *short axes*.

Figure S1 illustrates the possible orientations and the XRD patterns of the 7YHO film consisting of a ferroelectric orthorhombic phase ($Pca2_1$) for the determination of the film orientation in this study. The *x*- and *y*-axes are the in-plane

Received: February 27, 2024
Revised: June 29, 2024
Accepted: July 14, 2024
Published: July 25, 2024

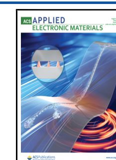

© 2024 The Authors. Published by American Chemical Society

Downloaded via NATL INST FOR MATLS SCIENCE (NIMS) on December 13, 2024 at 05:58:39 (UTC).
See https://pubs.acs.org/sharingguidelines for options on how to legitimately share published articles.

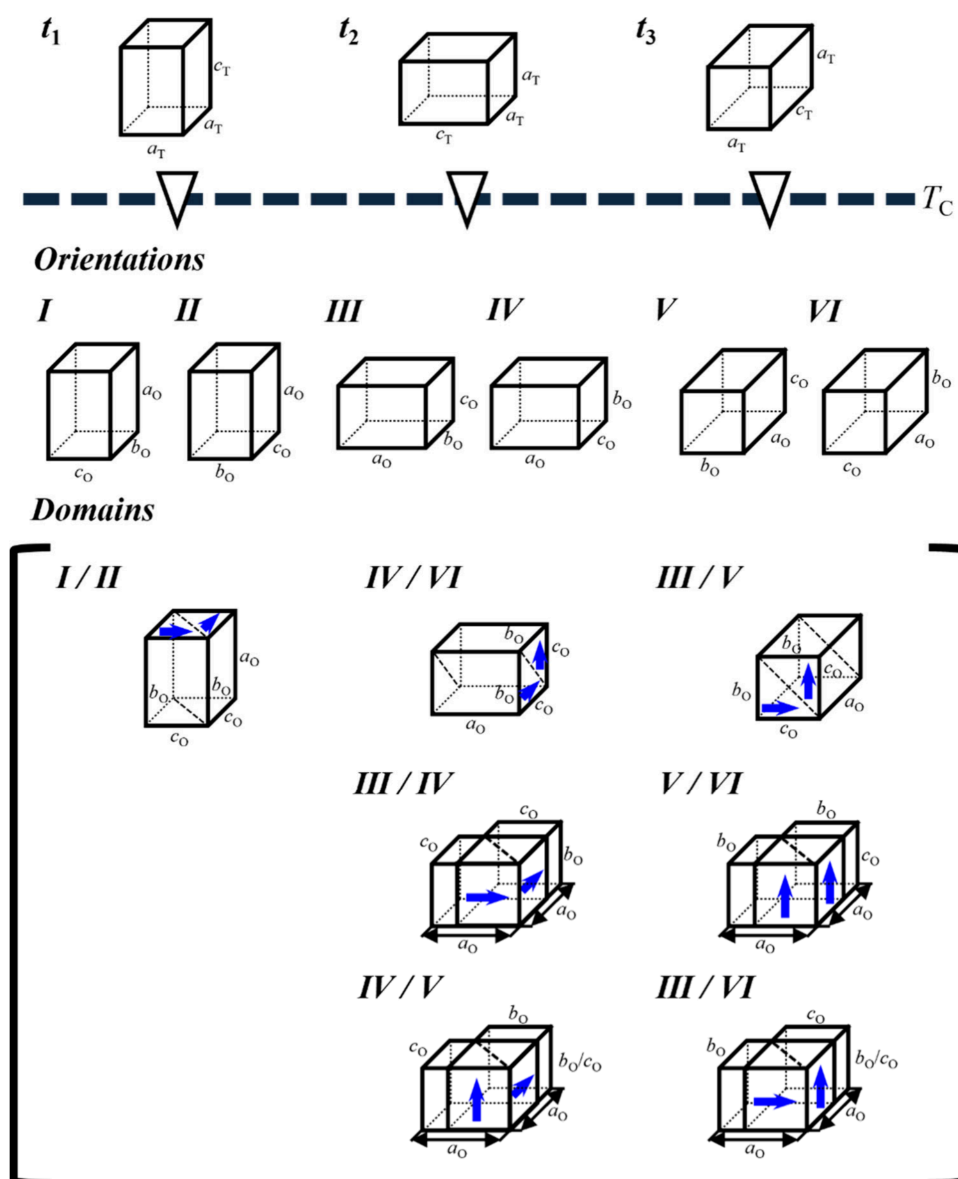

Figure 1. Schematic illustration of possible orientation and domain formation resulting from phase transition at the Curie temperature, T_c, from the high-temperature tetragonal to ferroelectric orthorhombic phase in epitaxial HfO_2 thin films. Here, domains having 180° domain relationships are not shown for simplification. This illustration was drawn based on the literature.[23,25,27]

directions and the z-axes are the out-of-plane direction on the substrate coordination (see Figure S1(a)). There are six possible orientations labeled as *orientation I−VI* shown in Figure S1(b), following the nomenclature in our previous report.[22] The crystal phase and the orientation were determined based on four types of XRD measurements: (1) $2\theta-\omega$ scans along the z-direction, (2) $2\theta-\psi$ scans along the y-z-direction, (3) $2\theta\chi-\varphi$ scans along the y-direction, and (4) $2\theta\chi-\varphi$ scans along the x-y-direction. An illustration of the scan directions, relevant lattice planes, and XRD patterns for the possible orientation of 7YHO can be found in Figure S1(c-f). The indices of Bragg diffraction and the angles corresponding to the XRD measurements are also shown. Note that the 2θ angles corresponding to these XRD measurements are shown in these figures based on the calculated values for $(Hf,Zr)O_2$ films.[21] The observations of 030 and 110 diffractions allow phase identification of the ferroelectric orthorhombic phase from the perspective of its reflection conditions[22] as $0kl$: $l = 2n$, $h0l$: $h = 2n$, $h00$: $h = 2n$, and $00l$: $l = 2n$, since the diffraction peaks corresponding to the 030 and 110 in the orthorhombic phase are not observed in the case of a higher symmetric tetragonal phase. The film orientation can be determined based on the appearance of such diffractions unique to the orthorhombic phase and difference in diffraction angles, e.g., between 200 and 020/002 as well. More detailed explanation of the measurements can be found in our previous report.[23]

EXPECTED ORIENTATION IN {100}-ORIENTED FILMS

High-temperature XRD analysis of the {100}-oriented 7YHO films revealed that the T_c was approximately 500 °C.[9] Note that during cooling after depositing the films at 700 °C, the tetragonal phase ($P4_2/nmc$) is converted to the orthorhombic phase ($Pca2_1$), after which domains can form, as discussed in the literature.[23−25] Note that the *long axis* direction differs for space groups $P4_2/nmc$ and $Pca2_1$. Throughout this report, we

https://doi.org/10.1021/acsaelm.4c00368
ACS Appl. Electron. Mater. 2024, 6, 5525−5535

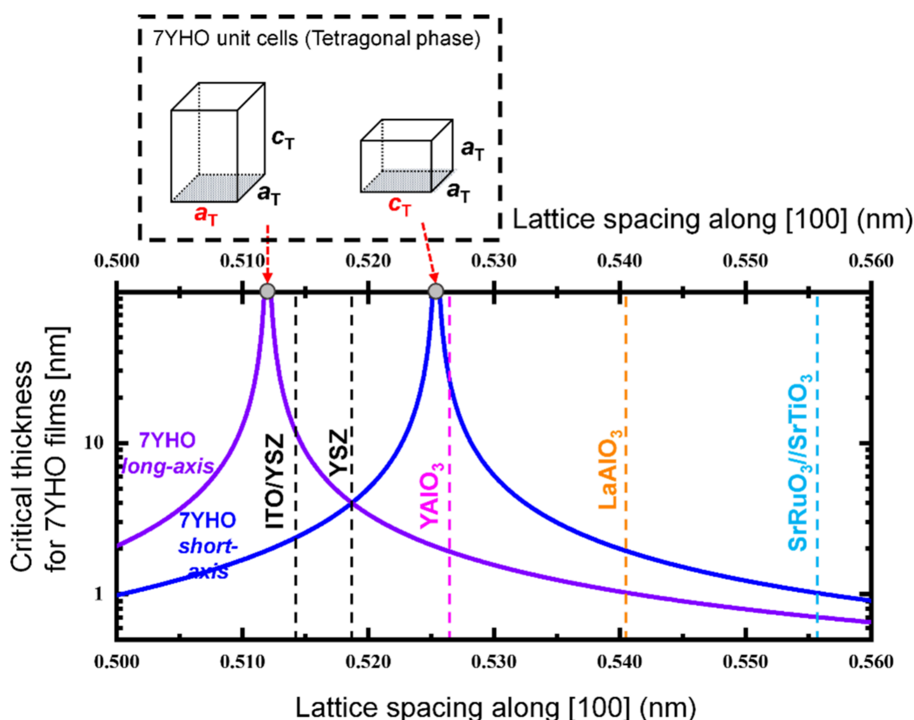

Figure 2. Theoretically calculated critical thickness of tetragonal 7% $YO_{1.5}$-93%HfO_2 (7YHO) film at 700 °C as a function of the lattice spacing along [100]. Blue line: the critical thickness of *short-axis*-oriented tetragonal 7YHO film, purple line: the thickness of *long-axis*-oriented tetragonal 7YHO film. The critical thicknesses were estimated based on the People and Bean theory.[28] A sketch of unit cells for the 7YHO and its lattice parameter were described in an inset. Calculated lattice parameters at 700 °C of relevant substrates are also shown.

use the description of *long axis* and *short axis* for the tetragonal phase in the same manner as for the orthorhombic phase: *long axis* denotes the c_T-axis and *short axis* denotes the a_T-axes. Figure S1 shows the possible crystallographic domains and the relationship between the tetragonal and orthorhombic phases. The (1) *short-axis*-oriented and (2) *long-axis*-oriented orthorhombics result from short-axis-oriented and long-axis-oriented tetragonal phases of 7YHO at high temperature.

(I) The out-of-plane *long-axis*-oriented orthorhombic films are obtained at room temperature (see *Orientation I–II* in Figures S1 and 1) when out-of-plane *long-axis*-oriented tetragonal films are grown at deposition temperatures above T_c. The polar axis (c_O-axis) lies in the in-plane direction.

(II) Out-of-plane *short-axis*-oriented orthorhombic films are expected to be obtained at room temperature (see *Orientation III-VI* in Figures S1 and 1) when out-of-plane *short-axis*-oriented tetragonal films are grown at the deposition temperature. It is known that the application of an electric field can induce polarization-switching from the in-plane to the out-of-plane direction in out-of-plane *short-axis*-oriented Y-doped HfO_2 films.[26] In this case, the polar axis can be oriented toward either the out-of-plane or in-plane direction, and its direction can be controlled by an external electric field.

Orientation control of the *long axis* and *short axis* in tetragonal films can be achieved by selecting the underlying layer based on the in-plane lattice parameters. We previously ascertained that *short-axis-* and *long-axis*-oriented orthorhombic films can be grown on (100)YSZ and $(100)_{pc}$ (indium−tin-oxide, ITO)//(100)YSZ substrates,[23] respectively. These observations suggest that there is a critical in-plane lattice parameter for the growth of *short-axis-* and *long-axis*-oriented films. In this study, a nominal film thickness of 20 nm was used for estimation of the critical thickness. The critical thickness for strain relaxation is an important indicator for the growth of coherently strained films. The estimated range for lattice matching with underlying layers was discussed with respect to the critical thickness for plastic relaxation in the next paragraph. Figure 2 shows the calculated critical thickness for the *long-axis-* and *short-axis*-oriented 7YHO films as a function of the lattice spacing of the underlying layer at a deposition temperature of 700 °C based on the model reported by People and Bean.[28] The lattice parameters of tetragonal 7YHO and various single-crystal substrates at the deposition temperature were estimated from the reported values at room temperature and the thermal expansion coefficient.[28] Those values are listed in Table S1.[23,29−37]

The approximate lattice matching range was estimated based on the People and Bean theory for plastic relaxation. As Hartmann et al. reported that real critical thicknesses often differ from the theoretically predicted value, the real critical thickness for strain relaxation, for example, the difference in the crystal structure between the perovskite structure and fluorite-like structure, can influence on the critical thickness.[38−41] The estimated ranges where strained films with thickness of below the critical thickness can be obtained are 0.524−0.527 nm and 0.511−0.513 nm for the in-plane *long axis* and *short axis*, respectively. Therefore, the 7YHO film on $YAlO_3$ is expected to adopt an out-of-plane *short-axis* orientation owing to the small lattice mismatch (below 0.1%) with respect to the in-plane *long axis*, whereas the orientation of the films on $LaAlO_3$ and $SrTiO_3$ cannot be estimated on this basis because of the relatively large in-plane lattice mismatch between the film and the substrates.

■ RESULTS

Direct Growth on Various Substrates. Figure 3 shows the out-of-plane XRD 2θ−ω scans near the {200} and {300}

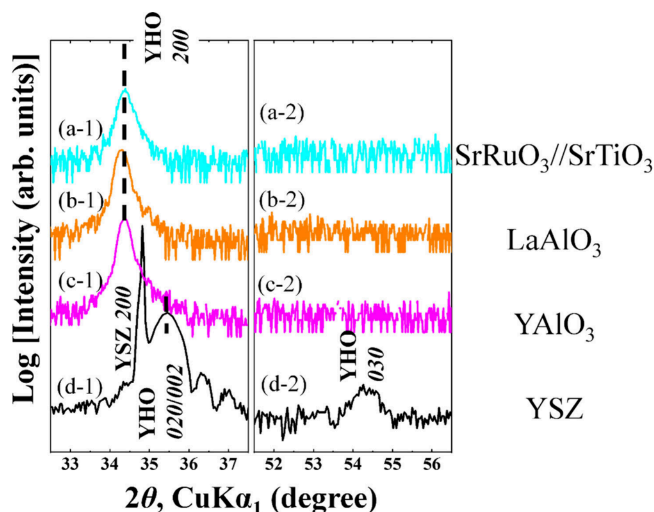

Figure 3. XRD 2θ−ω patterns near (1) {200} peaks and (2) {300} peaks for the 7YHO films grown on (a) $(100)_{pc}SrRuO_3/SrTiO_3$, (b) $(100)_{pc}LaAlO_3$, (c) $(100)_{pc}YAlO_3$, and (d) (100) YSZ substrates.

peaks of the 7YHO films grown on $(100)_{pc}SrRuO_3//SrTiO_3$, $(100)_{pc}LaAlO_3$, $(100)_{pc}YAlO_3$, and (100)YSZ substrates. The {200} peaks were observed for all of the films, whereas the 030 peak was observed only for the films on the (100)YSZ substrates. Taking into account the peak positions of 7YHO 200 at 2θ ≈ 34.4° (see Figure 3(a-1, b-1, c-1)), the orientations of the films, except that on YSZ, were identified as *long-axis* orientations (*Orientations I*−*II*). On the other hand, the films on YSZ possibly adopt the *short-axis* orientations (*Orientations III*−*IV* and/or *V*−*VI*), the identification of which is also supported by a fact that the 2θ peak position of 7YHO 020/002 is 35.4°.

Figure 4 shows the XRD 2θ−ψ scans for the 7YHO films. Note that the two XRD 2θ−ψ scans at different sample rotation angles φ (0° along $<110>_{pc}$ YHO and 45° along $<100>_{pc}$ YHO) are shown in the single maps. The 110 spots of the perovskite-structured substrates were observed in the scan areas framed by the dashed line. The observation of 110 spots at 2θ ≈ 24.7° and ψ ≈ 45° provides an indicator of the presence of the orthorhombic phase or monoclinic phase based on the reflection conditions. The 110 spots were observed when ψ > 45°, as shown in Figure 3(a−c), supporting the identification of the *long-axis* orientations (*Orientations I*−*II*) for the films, except for that on YSZ (Figure 4(a−c)). The XRD 2θ−ψ scan for the films on YSZ (Figure 4(d)) shows a 7YHO 110 spot at ψ < 45°, which is consistent with the *short-axis* orientations (*Orientations III*−*IV*) shown in Figure 3(d-1, 2).

Figure 5 displays the three kinds of in-plane XRD 2$\theta\chi$−φ scans for the 7YHO films: (1) near {200}, (2) {300} along the direction of $<100>_{pc}$YHO, and (3) near 110 along the direction of $<110>_{pc}$YHO. The films other than that on YSZ were also found to have *long-axis* orientations (*Orientation I* and/or *II*) based on observation of the in-plane {200} and 030 peaks, as displayed in Figure 5(a-1, b-1, c-1) and (a-2, b-2, c-2), respectively. The in-plane 110 peaks were not significantly observed in Figure 5(a-3, b-3, and c-3), indicating *Orientation I* and/or *II*. The same in-plane XRD 2$\theta\chi$−φ scans along the direction of $<010>_{pc}$YHO also showed in-plane 2 peaks; lower 2θ angle of 200 peak than {020} and 030 peaks as found in Figure 3(d-1) and (d-2). These results suggest the formation of an in-plane 90° domain with both *Orientation I* and *II*.

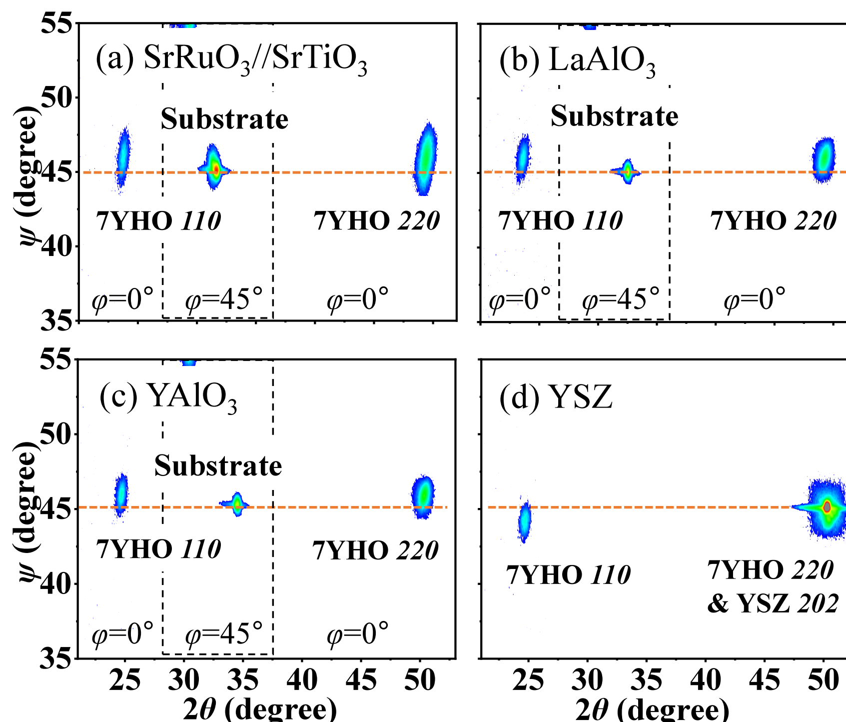

Figure 4. XRD 2θ−ψ patterns near the (1) {200} peak and (2) {300} peak for the 7YHO films grown on (a) $(100)_{pc}SrRuO_3/SrTiO_3$, (b) $(100)_{pc}LaAlO_3$, (c) $(100)_{pc}YAlO_3$, and (d) (100) YSZ substrates.

https://doi.org/10.1021/acsaelm.4c00368
ACS Appl. Electron. Mater. 2024, 6, 5525−5535

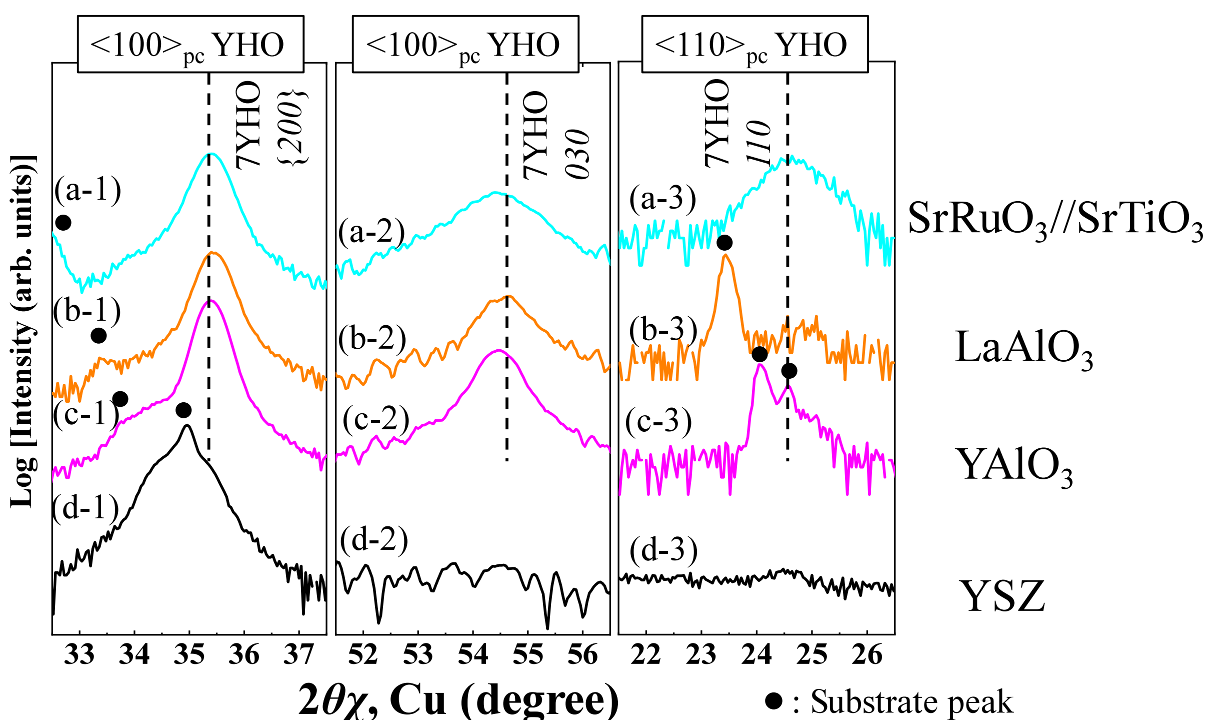

Figure 5. XRD $2\theta\chi-\varphi$ patterns near (1) {200} and (2) {300} peaks along the direction of <100>$_{pc}$ YHO and (3) near 110 peaks along the direction of <110>$_{pc}$ YHO for the 7YHO films grown on (a) $(100)_{pc}SrRuO_3/SrTiO_3$, (b) $(100)_{pc}LaAlO_3$, (c) $(100)_{pc}YAlO_3$, and (d) (100) YSZ substrates. Black circles show the substrate diffraction peaks.

However, the 030 and 110 peaks were of negligible intensity for the film on (100)YSZ, as shown in Figures 5(d-2 and d-3), respectively. These results indicate that the film on (100)YSZ has a single *short-axis* orientation (*Orientation III–IV*), with the polar axis aligned along the in-plane direction. The in-plane lattice parameters of the films on YSZ were almost the same as those on YSZ itself, suggesting that the in-plane lattice was almost clamped.

Difference in the *long-axis* lattice parameter of 7YHO and the corresponding lattice spacing of $YAlO_3$ can be estimated to be below 0.1%. Therefore, it was expected to grow with the out-of-plane, short-axis orientation on $YAlO_3$. However, 7YHO films exhibited an out-of-plane *long-axis orientation* experimentally.

Insertion of the Buffer Layer. The growth of the *long-axis*-oriented YHO films on $YAlO_3$ is inconsistent with the fact that the *short-axis*-oriented film exhibits a better lattice match with that of $YAlO_3$. Electrical matching at the interfaces is another factor that can affect the growth orientation. The crystal structures of 7YHO and $YAlO_3$ and their electrical matching were examined. Figure S2 shows schematic fluorite and perovskite structures drawn using VESTA.[42] The fluorite-type structure consists of alternating planes A and B, which are positively and negatively charged, respectively. The perovskite structure is composed by alternating planes A' and B'. The total charge of the respective plane is neutral for $SrTiO_3$, or charged for $YAlO_3$ and $LaAlO_3$, but the planes consist of both cations and anions. This suggests that the electrostatic potentials of the layers in these two structures are different with respect to total charge and local charge distribution. Thus, despite matching of the ionic positions of these two structures at the interface, the electrical matching of the ions is not as good when the 7YHO film is grown on the $YAlO_3$ substrate. This consideration suggests us that the insertion of the buffer layer with a pseudocubic fluorite structure and the same lattice parameter as $YAlO_3$ can form out-of-plane *short-axis*-oriented films by the matching the *long axis* of the 7YHO film along the in-plane direction.

Figure S3 shows the reported lattice parameters of $(A_xZr_{1-x})O_2$ (A = Ce,[43] Y,[44] Ca,[45] or Mg[45]) with a fluorite structure as a function of *x*. Here, the lattice parameters for $(A_xZr_{1-x})O_2$ with higher-symmetry phases, such as tetragonal and pseudocubic phases, were plotted. CeO_2 has a fluorite structure and can form a $(Ce_xZr_{1-x})O_2$ solid-solution over a wide *x* range, with cubic or pseudocubic symmetry. $(Ce_{0.35}Zr_{0.65})O_2$ (CZO) was selected as the buffer layer because its lattice parameter is close to the diagonal lattice spacing of $YAlO_3$ (0.522 nm).

The structural properties of approximately 15 nm thick CZO buffer layers epitaxially grown on $(100)_{pc}LaAlO_3$, $(100)_{pc}YAlO_3$, and (100)YSZ substrates were investigated. Here, $(100)_{pc}SrRuO_3//SrTiO_3$ was excluded because of the large lattice mismatch between the substrate and CZO required to obtain a coherently strained film, as shown in Figure S4. Figures S5 and S6 respectively show the out-of-plane XRD $2\theta-\omega$ scans and in-plane XRD $2\theta\chi-\varphi$ scans for the 10 nm thick CZO buffer layer on the substrates. The lattice spacings of the underlying layers increased sequentially for YSZ, $YAlO_3$, and $LaAlO_3$. In addition, it was found that the CZO film on the YSZ substrate showed stronger peak intensity than those on $YAlO_3$, and $LaAlO_3$ substrates. This might be because the consistency of the fluorite structure can result in better crystallinity and stronger intensity than the films grown on the perovskite-structured substrate. As shown in Figure S5, the out-of-plane lattice parameters of the CZO films decreased as the lattice spacing of the underlying layers increased. The in-plane lattice parameters of the CZO films increased as the lattice spacing of the underlying layers increased (Figure S6).

The peak positions of CZO {200} and $LaAlO_3$ {110} differed in the in-plane measurements (Figure S6(a)), suggesting strain relaxation of the CZO film from the substrate. In contrast, the peaks of CZO {200} and the $YAlO_3$ and YSZ substrates overlapped, as shown in Figure S6(b,c).

Figure S7 summarizes the in-plane lattice parameters of the CZO buffer layer, estimated from the in-plane XRD $2\theta\chi-\varphi$ scans (Figure S6), as a function of the in-plane lattice spacing of the underlying substrate. The lattice parameters of the buffer layers matched those of the $YAlO_3$ substrate and matched fairly well with those of the YSZ substrate, whereas the CZO film on $LaAlO_3$ was almost relaxed, because its in-plane lattice parameter was close to the reported value for the bulk, as indicated by the red dashed-dotted line in Figure S7. This trend can be explained by considering the critical thickness (Figure S4). The critical thicknesses of the CZO films on $YAlO_3$, YSZ, and $LaAlO_3$ were estimated to be 15, 3, and 2 nm, respectively. Consequently, fluorite-structured CZO buffer layers with different lattice spacings between YSZ and bulk CZO were successfully fabricated. Based on the obtained lattice spacings, *short-axis*-oriented 7YHO films can be grown and their lattice strain can be controlled.

Film Growth on the Buffer Layer. Figure 6 shows the out-of-plane XRD $2\theta-\omega$ scans near the {200} and {300} peaks

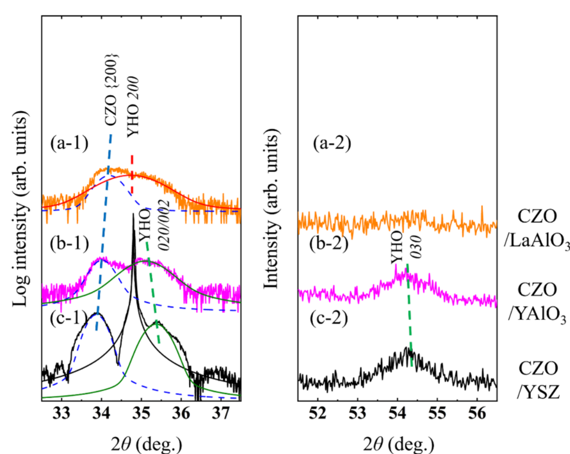

Figure 6. XRD $2\theta-\omega$ patterns near (1) {200} and (2) {300} peaks for 7YHO films grown on (a) CZO-buffered $(100)_{pc}LaAlO_3$, (b) CZO-buffered $(100)_{pc}YAlO_3$, and (c) CZO-buffered (100) YSZ substrates. Blue dashed lines: based on the CZO {200} peak shown in Figure S5, green lines: 7YHO 020/002 peak, red lines: 7YHO 200 peak.

for the films on CZO-buffered $(100)_{pc}LaAlO_3$, $(100)_{pc}YAlO_3$, and (100)YSZ. The XRD profiles were fitted by using multiple Gaussian functions. The peak positions of the CZO buffer layers were assumed based on the results shown in Figure S5. A 7YHO 200 peak was observed for the film on the CZO-buffered $LaAlO_3$, whereas the 020/002 and 030 peaks were not clearly observed. The existence of the *long-axis* orientation (*Orientations I* and/or *II*) for the films on CZO-buffered $LaAlO_3$ is suggestive considering the 7YHO {200} peak positions, but the existence of the short-axis orientation should be carefully considered with other XRD scans. However, the 020/002 and 030 peaks were both observed, indicating that the films on CZO-buffered $YAlO_3$ and CZO-buffered YSZ may adopt a *short-axis* orientation (*Orientations III*−*IV* and/or *V*−*VI*).

Figure 7 shows the composite XRD $2\theta-\psi$ scans for the 7YHO films, analogous to that in Figure 4. The presence of the orthorhombic phase in all of the films was confirmed by the observation of 110 spots. The 7YHO 110 spots of the films on CZO-buffered $YAlO_3$ and CZO-buffered YSZ were most intense with $\psi < 45°$, also indicating the *short-axis* orientation (*Orientations III*−*IV* and/or *V*−*VI*). Remarkably, the ψ angle information corroborates the absence of the *long-axis* orientation of 7YHO, which is hidden by the diffraction peaks of the CZO buffer layer in Figure 6.

Figure 8 shows three types of in-plane XRD $2\theta\chi-\varphi$ scans for the 7YHO film: (1) near {200}, (2) {300} along the direction of $<100>_{pc}$ YHO, and (3) near 110 along the direction of $<110>_{pc}$ YHO. The XRD profiles were fitted to multiple Gaussian functions, and the peak positions of the buffer layers were assumed based on the results in Figure S6. The peaks of the substrates were calculated from the following lattice constants: a = 0.536 nm for $LaAlO_3$, a = 0.522 nm for $YAlO_3$, and a = 0.514 nm for YSZ.

The measurements for the film on CZO-buffered $(100)_{pc}LaAlO_3$ showed the presence of 7YHO 020/002 and 7YHO 030 peaks but no 7YHO 110 peak. These results correspond to *Orientations I*−*II*, the coexistence of which was confirmed by the observation of the 030 peak in the in-plane XRD $2\theta\chi-\varphi$ scans along the direction $<010>_{pc}$ of YHO.

For the films on CZO-buffered $(100)_{pc}YAlO_3$ and CZO-buffered (100)YSZ, the observation of both the 7YHO 200 and 7YHO 020/002 peaks indicates that the films have *short-axis* and *long-axis* orientation in the in-plane direction (Figures 6 and 8). YHO 030 and 7YHO 110 peaks were also observed. The data indicate *Orientation V*−*VI*. These results are not inconsistent with the deduction of *Orientation III*−*IV* based on the out-of-plane XRD $2\theta-\omega$ scans in Figure 6. In summary, XRD analysis of the films on CZO-buffered $(100)_{pc}YAlO_3$ and CZO-buffered (100)YSZ confirmed the existence of *Orientations III*, *IV*, *V*, and *VI*, suggesting the existence of a 90° polydomain structure (see also Figure 1). The data differ from the results for the film deposited directly on YSZ, where only *Orientations III* and *IV* were present in the in-plane 90° domain.

■ DISCUSSION

Figure 9 shows the out-of-plane and in-plane lattice parameters of 7YHO, calculated from the XRD $2\theta-\omega$ and $2\theta\chi-\varphi$ scans, respectively, as a function of the lattice spacing of the underlying layer. Table 1 shows the calculated lattice parameters and orientation of the 7YHO films on each substrate. *Short-axis*-oriented 7YHO films were obtained when the in-plane lattice parameter was in the range of 0.518−0.523 nm, where the lattice mismatch with the *long axis* ranged from −1.8% to −0.2%, as shown in Figure 9. Selective growth of the *long-axis*-oriented 7YHO films was achieved by selecting an underlying layer with a lattice spacing >0.525 nm or lattice mismatch with the *long-axis* > 0.8%. Lattice strain relaxation was observed in these *long-axis*-oriented films, which resulted in almost relaxed *short-axis* and *long-axis* lattice parameters of 0.506 and 0.523 nm, respectively. It was reported that epitaxial unstrained (111)-oriented films of ferroelectric $(Hf,Zr)O_2$ on strain-controlled $(La,Sr)MnO_3$ electrodes grow epitaxially through an unconventional mechanism of epitaxy. Meanwhile, the observation of unclamped lattice parameters for orthorhombic HfO_2-based materials was experimentally achieved in different (100) orientation films in this work.

https://doi.org/10.1021/acsaelm.4c00368
ACS Appl. Electron. Mater. 2024, 6, 5525−5535

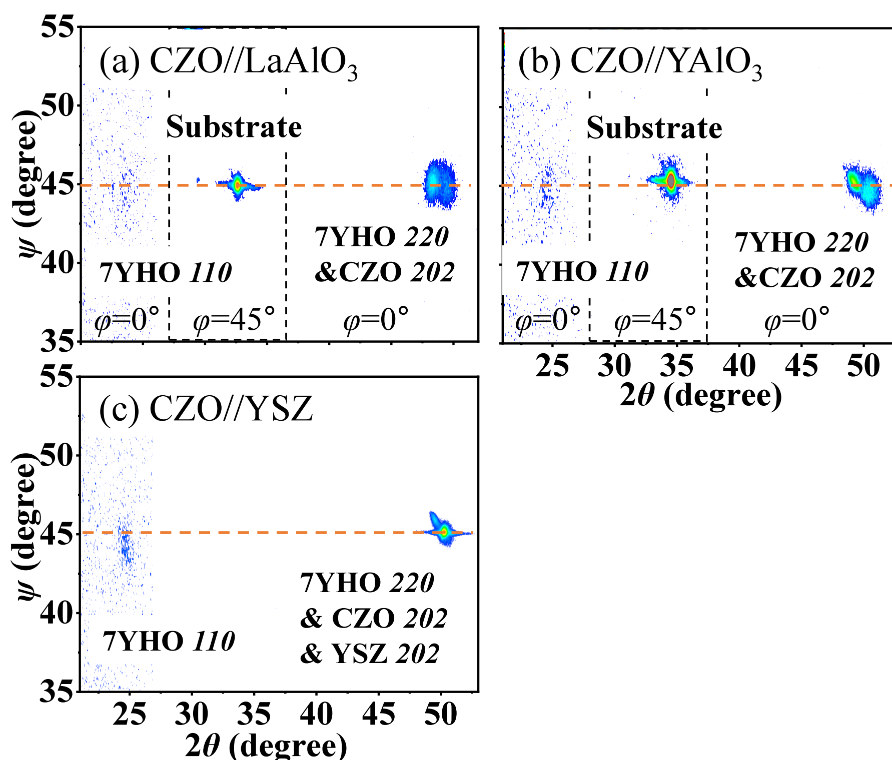

Figure 7. XRD $2\theta-\psi$ patterns of 7YHO films and the CZO buffer layer deposited on (a) $(100)_{pc}LaAlO_3$, (b) $(100)_{pc}YAlO_3$, and (c) (100) YSZ substrates. The dotted line shows a tilt angle of 45°. The area framed by the dashed line is the area where the 110 spots of the perovskite structure substrates were observed by rotating the film 45° in the φ direction.

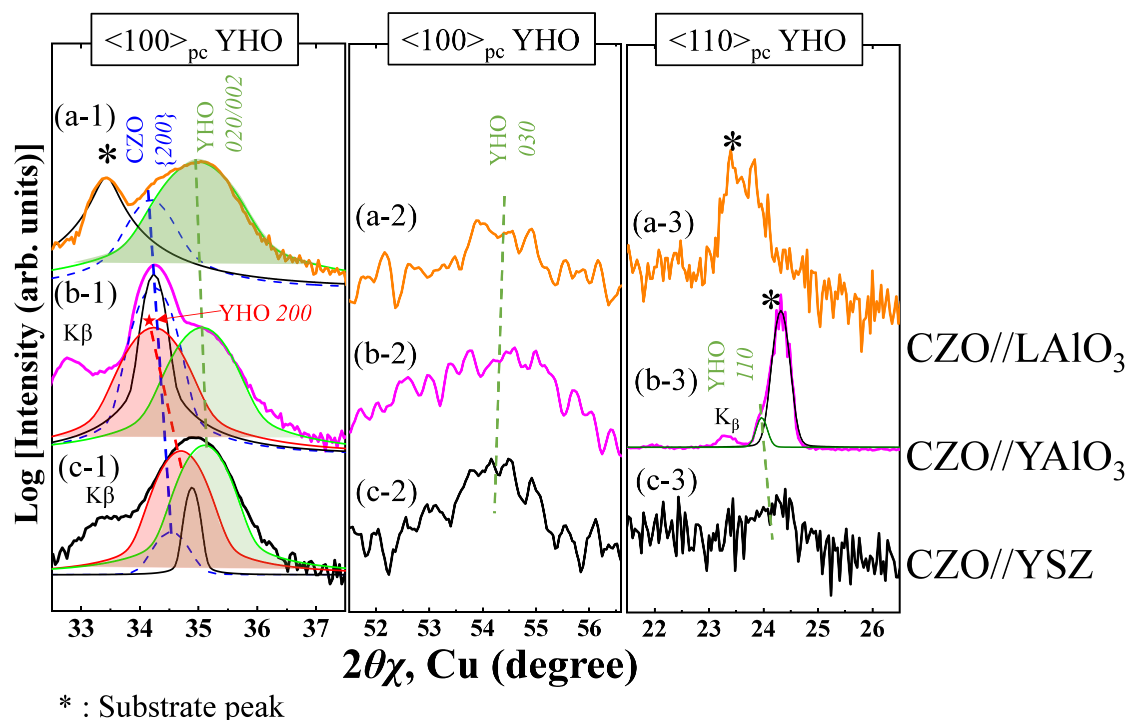

Figure 8. XRD $2\theta\chi-\varphi$ patterns near (1) {200} and (2) {300} peaks along the direction of <100>$_{pc}$ YHO and (3) near 110 peaks along the direction of <110>$_{pc}$ YHO for the 7YHO films grown on (a) $(100)_{pc}LaAlO_3$, (b) $(100)_{pc}YAlO_3$, and (c) (100) YSZ substrates. Blue fitting lines: $(Ce_{0.35}Zr_{0.65})O_2$ peak {200}, green lines: 7YHO 020/002 peak, 7YHO 030 peak, and red lines: 7YHO 200 peak.

The growth range of *short-axis*-oriented films is limited. The growth of *long-axis*-oriented films with a large lattice mismatch can be explained by the anisotropy of the imposed strain: isotropic biaxial strain is imposed on the *long-axis*-oriented films and anisotropic strain is imposed on the *short-axis*-oriented films. As shown in Figure 5(d), YSZ has a lattice parameter of 0.518 nm, which lies between the *long* axis c_T and the *short axes* a_T. Considering that the in-plane lattice

https://doi.org/10.1021/acsaelm.4c00368
ACS Appl. Electron. Mater. 2024, 6, 5525−5535

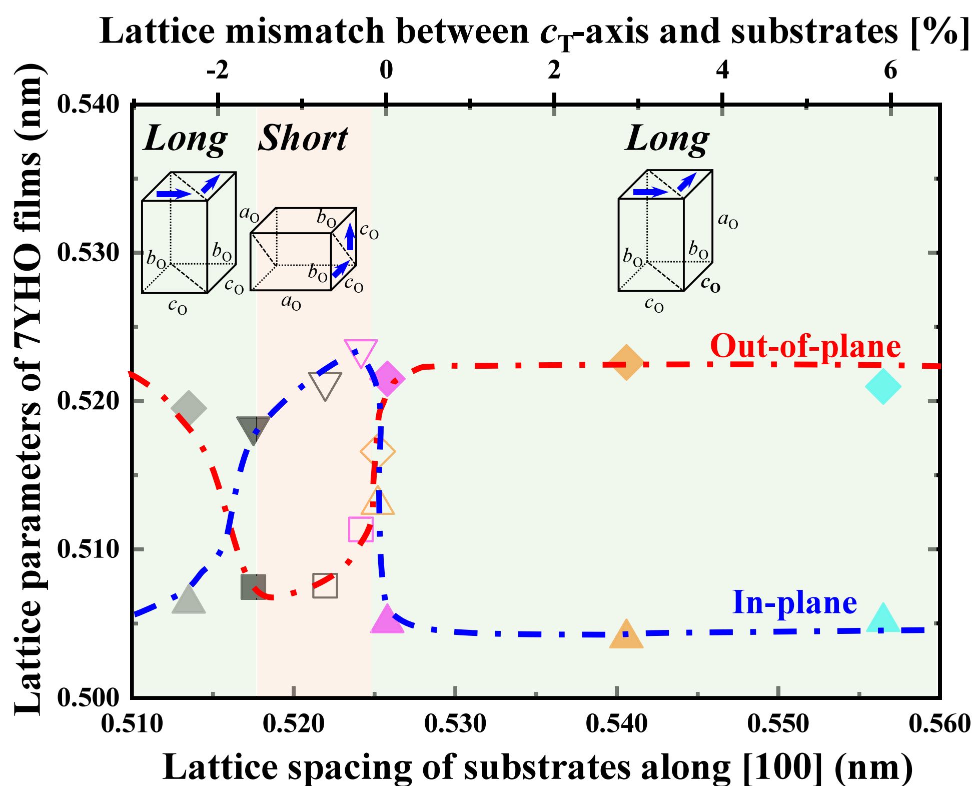

Figure 9. Lattice parameter of 7YHO films as a function of substrate lattice spacing along [100] at the deposition temperature of 700 °C. Closed symbols: films grown directly on substrates; open symbols: $(Ce_{0.35}Zr_{0.65})O_2$-buffered substrates; square symbols: out-of-plane lattice parameters of *long-axis*-oriented films; diamond symbols: out-of-plane lattice parameters of *short-axis*-oriented films; inverse triangle symbols: in-plane lattice parameters of *long-axis*-oriented films; triangle symbols: in-plane lattice parameters of *short-axis*-oriented films. The dashed dotted lines represent the out-of-plane lattice parameter (red line) and the in-plane lattice parameter (blue line).

Table 1. Calculated Lattice Parameters and Orientation of 7YHO Films on Each Substrate

Substrate	Out-of-plane lattice parameter of 7YHO film [nm]	In-plane lattice parameter of 7YHO film [nm]	7YHO film orientation
ITO//YSZ	0.520	0.506	(100)
YSZ	0.507	0.518	(010)
$YAlO_3$	0.522	0.505	(100)
$LaAlO_3$	0.523	0.504	(100)
$SrRuO_3$//$SrTiO_3$	0.521	0.505	(100)
CZO//YSZ	0.508	0.521	(010)/(001)
CZO//$YAlO_3$	0.511	0.523	(010)/(001)
CZO//$LaAlO_3$	0.517	0.513	(100)

parameter of the films on YSZ was almost the same as that of YSZ, anisotropic strain (i.e., tensile strain) was imposed on the *short axis* c_o and compressive strain was imposed on the *long axis* a_o. Anisotropic strain with tensile strain on the *short axis* c_o and *long axis* a_o is not energetically favorable, as experimentally shown by the growth of the *long-axis* under an isotropic tensile strain. One can easily imagine that the strain relaxation due to domain formation can possibly occur to decrease the elastic energy penalty of lattice mismatching and to lower the thickness where strain relaxation takes place, as described as domain III/IV, IV/V, V/VI, and III/VI in Figure 1. For this clarification, further studies with high-resolution transmission electron microscopy are needed. Nevertheless, the trend of growth orientation can be understood in terms of lattice matching.

The growth orientation of films may be affected by other factors. As Speck mentioned, the depolarization field can contribute lattice strain relaxation or ferroelectric domain formation, and the extent of the depolarization fields depends on the insulating substrate or conductive substrate.[39−41] Therefore, it is probable that the resultant remnant strain on conductive buffer layers differs from this study. Although the film adopted *short-axis* b_o orientation (*Orientations III−IV*) in this study, both *short-axis* b_o and c_o orientations were coexistent in the films (*Orientations III−IV* and/or *V−VI*) in a previous report.[22] This may be caused by the difference in the deposition conditions, film thickness, or conductivity of underlying films; thus, these influences need to be further investigated in the future.

In addition to demonstrating orientation-selective growth, it is worth mentioning that the lattice strain for the *short-axis*- and *long-axis*-oriented 7YHO films is governed by the lattice spacing of the underlying layers. Manipulation of the lattice spacing using CZO buffer layers provides a window for film growth with a *short-axis* orientation and control of the strain state. Orientation control on electrodes is very important to understand the more detailed information. Based on the present result, further investigation of the growth on various conductive materials with suitable lattice matching is necessary. In addition, the electrical properties of the strained 7YHO films will be investigated as the next step.

https://doi.org/10.1021/acsaelm.4c00368
ACS Appl. Electron. Mater. 2024, 6, 5525−5535

■ CONCLUSIONS

{100}-Oriented, epitaxial, orthorhombic $(Hf_{0.93}Y_{0.07})O_2$ (7YHO) films were grown at 700 °C on various substrates, with and without $(Ce_{0.35}Zr_{0.65})O_2$ (CZO) buffer layers, using pulsed laser deposition. XRD measurements revealed that out-of-plane *short-axis*-oriented films were obtained on (100)YSZ, CZO-buffered $(100)_{pc}YAlO_3$, and CZO-buffered (100)YSZ substrates, whereas out-of-plane *long-axis*-oriented films were obtained on $(100)_{pc}SrRuO_3//SrTiO_3$, $(100)_{pc}LaAlO_3$, and $(100)_{pc}YAlO_3$ substrates. The unclamped lattice constants of the *short* and *long axes* (0.506 and 0.523 nm, respectively) of the orthorhombic 7YHO films were experimentally observed for the first time on $(100)_{pc}SrRuO_3//SrTiO_3$, $(100)_{pc}LaAlO_3$, and $(100)_{pc}YAlO_3$. *Short-axis*-oriented 7YHO films were obtained when the in-plane lattice parameter was within the range of 0.518−0.523 nm. The lattice parameters were controlled by inserting CZO buffer layers. Consequently, {100} orientation control and manipulation of the lattice strain were achieved by modulating the in-plane lattice spacing of the underlying layers. These findings provide a basis for understanding the fundamental ferroelectric properties of HfO_2-based materials.

■ EXPERIMENTAL METHODS

Epitaxial $(Hf_{0.93}Y_{0.07})O_2$ (7YHO) films with thickness ranging from 10 to 20 nm were grown at 700 °C under an oxygen pressure of 10 mTorr by pulsed laser deposition using a KrF excimer laser (λ = 248 nm). The power and repetition of KrF excimer laser were 35 mJ and 3 Hz, respectively, and the laser was focused on the target with an optical lens. The target-to-substrate distance of 55 mm was used. Single crystals of (100)YSZ, $(100)_{pc}YAlO_3$, $(100)_{pc}LaAlO_3$, and $(100)SrTiO_3$ covered by $(100)_{pc}SrRuO_3$ were used as substrates. The epitaxial $SrRuO_3$ film was deposited by radio frequency magnetron sputtering.

Approximately 15 nm thick epitaxial $(Ce_{0.35}Zr_{0.65})O_2$ buffer layers were grown before the deposition of 7YHO films. The deposition of $(Ce_{0.35}Zr_{0.65})O_2$ layers was implemented by using pulsed laser deposition. The laser condition, deposition temperature, oxygen pressure, and the target-to-substrate distance were same as for the deposition of 7YHO.

The crystal phase and the orientation were determined based on four types of XRD measurements: (1) $2\theta-\omega$ scans along the z-direction (PANalytical X'Pert MRD system), (2) $2\theta-\psi$ scans along the y-z-direction (Bruker, D8-discover), (3) $2\theta\chi-\varphi$ scans along the y-direction (Rigaku Smartlab), and (4) $2\theta\chi-\varphi$ scans along the x-y direction (Rigaku Smartlab). An X-ray diffractometer (Bruker, D8-discover) equipped with a large-area 2D detector (Vantec-500) with CuKα radiation was also used to evaluate the in-plane and out-of-plane crystal structure. In the in-plane XRD measurements, the parallel Soller slit with 0.5°, which is relatively wider than typically used, was employed to achieve observation of faint signals of diffraction peaks from the orthorhombic 7YHO. The orientation determination based on these XRD measurements was illustrated in Figure S1.

■ ASSOCIATED CONTENT

Supporting Information

The Supporting Information is available free of charge at https://pubs.acs.org/doi/10.1021/acsaelm.4c00368.

Additional experiments, schematics of the crystal orientations and domains, unit cells, lattice parameters of $(A_xZr_{1-x})O_2$ (fluorite structure) as a function of x, the calculated critical thickness of $(Ce_{0.35}Zr_{0.65})O_2$ films, out-of-plane and in-plane XRD patterns, and in-plane lattice spacing of the buffer layer as a function of the lattice spacing of the substrate (PDF)

■ AUTHOR INFORMATION

Corresponding Authors

Hiroshi Funakubo − *Department of Materials Science and Engineering, Tokyo Institute of Technology, Yokohama, Kanagawa 226-8502, Japan;* orcid.org/0000-0002-1106-200X; Email: funakubo.h.aa@m.titech.ac.jp

Kazuki Okamoto − *Department of Materials Science and Engineering, Tokyo Institute of Technology, Yokohama, Kanagawa 226-8502, Japan;* Email: okamoto.k.ar@m.titech.ac.jp

Authors

Yoshiki Maekawa − *Department of Materials Science and Engineering, Tokyo Institute of Technology, Yokohama, Kanagawa 226-8502, Japan*

Koji Hirai − *Department of Materials Science and Engineering, Tokyo Institute of Technology, Yokohama, Kanagawa 226-8502, Japan*

Takao Shimizu − *National Institute for Materials Science, Tsukuba, Ibaraki 987-6543, Japan;* orcid.org/0000-0001-9508-7601

Complete contact information is available at: https://pubs.acs.org/10.1021/acsaelm.4c00368

Author Contributions

The manuscript was written through contributions of all authors. All authors have given approval to the final version of the manuscript.

Notes

The authors declare no competing financial interest.

■ ACKNOWLEDGMENTS

This work was supported by the MEXT Initiative to Establish Next-Generation Novel Integrated Circuits Centers (X-NICS) (JPJ011438), the MEXT Program: Data Creation and Utilization Type Material Research and Development (JPMXP1122683430), and by the Japan Society for the Promotion of Science (JSPS) KAKENHI Grant Nos. 21H01617, 22K18307, 23K13364, and 24H00375.

■ REFERENCES

(1) Müller, J.; Böscke, T. S.; Bräuhaus, D.; Schröder, U.; Böttger, U.; Sundqvist, J.; Kücher, P.; Mikolajick, T.; Frey, L. Ferroelectric $Zr_{0.5}Hf_{0.5}O_2$ Thin Films for Nonvolatile Memory Applications. *Appl. Phys. Lett.* **2011**, *99* (11), 112901.

(2) Müller, J.; Böscke, T. S.; Müller, S.; Yurchuk, E.; Polakowski, P.; Paul, J.; Martin, D.; Schenk, T.; Khullar, K.; Kersch, A.; Weinreich, W.; Riedel, S.; Seidel, K.; Kumar, A.; Arruda, T. M.; Kalinin, S. V.; Schlösser, T.; Boschke, R.; van Bentum, R.; Schröder, U.; Mikolajick, T. Ferroelectric Hafnium Oxide: A CMOS-Compatible and Highly Scalable Approach to Future Ferroelectric Memories. *IEEE Int. Electron Devices Meet.* **2013**, *2013*, 10.8.1−10.8.4.

(3) Boscke, T. S.; Muller, J.; Brauhaus, D.; Schroder, U.; Bottger, U. Ferroelectricity in Hafnium Oxide: CMOS Compatible Ferroelectric Field Effect Transistors. *Int.Electron Devices Meet.* **2011**, *2011*, 24.5.1−24.5.4.

(4) Cheema, S. S.; Shanker, N.; Hsu, C.; Datar, A.; Bae, J.; Kwon, D.; Salahuddin, S. One Nanometer HfO_2-Based Ferroelectric Tunnel Junctions on Silicon. *Adv. Electron. Mater.* **2022**, *8* (6), 2100499.

(5) Gao, Z.; Luo, Y.; Lyu, S.; Cheng, Y.; Zheng, Y.; Zhong, Q.; Zhang, W.; Lyu, H. Identification of Ferroelectricity in a Capacitor

With Ultra-Thin (1.5-Nm) $Hf_{0.5}Zr_{0.5}O_2$ Film. *IEEE Electron Device Lett.* **2021**, *42* (9), 1303−1306.

(6) Mikolajick, T.; Slesazeck, S.; Mulaosmanovic, H.; Park, M. H.; Fichtner, S.; Lomenzo, P. D.; Hoffmann, M.; Schroeder, U. Next Generation Ferroelectric Materials for Semiconductor Process Integration and Their Applications. *J. Appl. Phys.* **2021**, *129* (10), 100901.

(7) Gong, N.; Ma, T.-P. Why Is FE−HfO2More Suitable Than PZT or SBT for Scaled Nonvolatile 1-T Memory Cell? A Retention Perspective. *IEEE Electron Device Lett.* **2016**, *37* (9), 1123−1126.

(8) Lee, Y.; Broughton, R. A.; Hsain, H. A.; Song, S. K.; Edgington, P. G.; Horgan, M. D.; Dowden, A.; Bednar, A.; Lee, D. H.; Parsons, G. N.; Park, M. H.; Jones, J. L. The Influence of Crystallographic Texture on Structural and Electrical Properties in Ferroelectric $Hf_{0.5}Zr_{0.5}O_2$. *J. Appl. Phys.* **2022**, *132* (24), 244103.

(9) Tashiro, Y.; Shimizu, T.; Mimura, T.; Funakubo, H. Comprehensive Study on the Kinetic Formation of the Orthorhombic Ferroelectric Phase in Epitaxial Y-Doped Ferroelectric HfO_2 Thin Films. *ACS Appl. Electron. Mater.* **2021**, 3 (7), 3123−3130.

(10) Zhang, S.; Yi, S.; Yang, J.-Y.; Liu, J.; Liu, L. Correlation between Spontaneous Polarization and Thermal Conductivity in Ferroelectric HfO2 from First Principles. *Int. J. Heat Mass Transfer* **2023**, *207*, No. 123971.

(11) Wei, W.; Zhao, G.; Zhan, X.; Zhang, W.; Sang, P.; Wang, Q.; Tai, L.; Luo, Q.; Li, Y.; Li, C.; Chen, J. Switching Pathway-Dependent Strain-Effects on the Ferroelectric Properties and Structural Deformations in Orthorhombic HfO2. *J. Appl. Phys.* **2022**, *131* (15), 154101.

(12) Mimura, T.; Tashiro, Y.; Shimizu, T.; Funakubo, H. Systematic Investigation of Ferroelectric Properties in $X\%YO_{1.5}-(100-X\%)$-$Hf_{1-y}Zr_yO_2$ Films. *ACS Appl. Electron. Mater.* **2023**, *5* (3), 1600−1605.

(13) Lee, Y.; Jeong, H. W.; Kim, S. H.; Yang, K.; Park, M. H. Effect of Stress on Fluorite-Structured Ferroelectric Thin Films for Semiconductor Devices. *Mater. Sci. Semicond. Process.* **2023**, *160*, No. 107411.

(14) Choi, K. J.; Biegalski, M.; Li, Y. L.; Sharan, A.; Schubert, J.; Uecker, R.; Reiche, P.; Chen, Y. B.; Pan, X. Q.; Gopalan, V.; Chen, L.-Q.; Schlom, D. G.; Eom, C. B. Enhancement of Ferroelectricity in Strained $BaTiO_3$ Thin Films. *Science* **2004**, *306* (5698), 1005−1009.

(15) Katayama, K.; Shimizu, T.; Sakata, O.; Shiraishi, T.; Nakamura, S.; Kiguchi, T.; Akama, A.; Konno, T. J.; Uchida, H.; Funakubo, H. Growth of (111)-Oriented Epitaxial and Textured Ferroelectric Y-Doped HfO_2 Films for Downscaled Devices. *Appl. Phys. Lett.* **2016**, *109* (11), 112901.

(16) Lyu, J.; Fina, I.; Solanas, R.; Fontcuberta, J.; Sánchez, F. Robust Ferroelectricity in Epitaxial $Hf_{1/2}Zr_{1/2}O_2$ Thin Films. *Appl. Phys. Lett.* **2018**, *113* (8), No. 082902.

(17) Estandía, S.; Dix, N.; Gazquez, J.; Fina, I.; Lyu, J.; Chisholm, M. F.; Fontcuberta, J.; Sánchez, F. Engineering Ferroelectric $Hf_{0.5}Zr_{0.5}O_2$ Thin Films by Epitaxial Stress. *ACS Appl. Electron. Mater.* **2019**, *1* (8), 1449−1457.

(18) Shimizu, T.; Katayama, K.; Kiguchi, T.; Akama, A.; Konno, T. J.; Funakubo, H. Growth of Epitaxial Orthorhombic $YO_{1.5}$-Substituted HfO_2 Thin Film. *Appl. Phys. Lett.* **2015**, *107* (3), No. 032910.

(19) Lee, K.; Lee, T. Y.; Yang, S. M.; Lee, D. H.; Park, J.; Chae, S. C. Ferroelectricity in Epitaxial Y-Doped HfO_2 Thin Film Integrated on Si Substrate. *Appl. Phys. Lett.* **2018**, *112* (20), 202901.

(20) Li, T.; Ye, M.; Sun, Z.; Zhang, N.; Zhang, W.; Inguva, S.; Xie, C.; Chen, L.; Wang, Y.; Ke, S.; Huang, H. Origin of Ferroelectricity in Epitaxial Si-Doped HfO_2 Films. *ACS Appl. Mater. interfaces* **2019**, *11* (4), 4139−4144.

(21) Materlik, R.; Künneth, C.; Kersch, A. The Origin of Ferroelectricity in $Hf_{1-x}Zr_xO_2$: A Computational Investigation and a Surface Energy Model. *J. Appl. Phys.* **2015**, *117* (13), 134109.

(22) Hahn, T. International Tables for Crystallography Volume A, Space-group symmetry. *Int. Tables Crystallogr.* **2006**, *A*, 17−41.

(23) Katayama, K.; Shimizu, T.; Sakata, O.; Shiraishi, T.; Nakamura, S.; Kiguchi, T.; Akama, A.; Konno, T. J.; Uchida, H.; Funakubo, H. Orientation Control and Domain Structure Analysis of {100}-Oriented Epitaxial Ferroelectric Orthorhombic HfO2-Based Thin Films. *J. Appl. Phys.* **2016**, *119* (13), 134101.

(24) Roytburd, A. L.; Ouyang, J.; Artemev, A. Polydomain Structures in Ferroelectric and Ferroelastic Epitaxial Films. *J. Phys.: Condens. Matter* **2017**, *29* (16), No. 163001.

(25) Ding, W.; Zhang, Y.; Tao, L.; Yang, Q.; Zhou, Y. The Atomic-Scale Domain Wall Structure and Motion in HfO_2-Based Ferroelectrics: A First-Principle Study. *Acta Mater.* **2020**, *196*, 556−564.

(26) Shimizu, T.; Mimura, T.; Kiguchi, T.; Shiraishi, T.; Konno, T.; Katsuya, Y.; Sakata, O.; Funakubo, H. Ferroelectricity Mediated by Ferroelastic Domain Switching in HfO_2 -Based Epitaxial Thin Films. *Appl. Phys. Lett.* **2018**, *113* (21), 212901.

(27) Kiguchi, T.; Shiraishi, T.; Shimizu, T.; Funakubo, H.; Konno, T. J. Domain Orientation Relationship of Orthorhombic and Coexisting Monoclinic Phases of $YO_{1.5}$-Doped HfO_2 Epitaxial Thin Films. *Jpn. J. Appl. Phys.* **2018**, *57* (11S), 11UF16.

(28) People, R.; Bean, J. C. Calculation of Critical Layer Thickness versus Lattice Mismatch for Ge_xSi_{1-x}/Si Strained-Layer Heterostructures. *Appl. Phys. Lett.* **1985**, *47* (3), 322−324.

(29) Kisi, E. H.; Howard, C. J.; Hill, R. J. Crystal Structure of Orthorhombic Zirconia in Partially Stabilized Zirconia. *J. Am. Ceram. Soc.* **1989**, *72* (9), 1757−1760.

(30) Yashima, M.; Takahashi, H.; Ohtake, K.; Hirose, T.; Kakihana, M.; Arashi, H.; Ikuma, Y.; Suzuki, Y.; Yoshimura, M. Formation of Metastable Forms by Quenching of the $HfO_2RO_{1.5}$ Melts (R = Gd, Y and Yb). *J. Phys. Chem. Solids* **1996**, *57* (3), 289−295.

(31) Ross, N. L.; Zhao, J.; Angel, R. J. High-Pressure Single-Crystal X-Ray Diffraction Study of $YAlO_3$ Perovskite. *J. Solid State Chem.* **2004**, *177* (4−5), 1276−1284.

(32) Chaix-Pluchery, O.; Chenevier, B.; Robles, J. J. Anisotropy of Thermal Expansion in $YAlO_3$ and $NdGaO_3$. *Appl. Phys. Lett.* **2005**, *86* (25), 251911.

(33) Lehnert, H.; Boysen, H.; Schneider, J.; Frey, F.; Hohlwein, D.; Radaelli, P.; Ehrenberg, H. A Powder Diffraction Study of the Phase Transition in $LaAlO_3$. *Z. für Krist. - Cryst. Mater.* **2000**, *215* (9), 536−541.

(34) da Silva, C. A.; de Miranda, P. E. V. Synthesis of $LaAlO_3$ Based Materials for Potential Use as Methane-Fueled Solid Oxide Fuel Cell Anodes. *Int. J. Hydrogen Energy* **2015**, *40* (32), 10002−10015.

(35) Culbertson, C. M.; Flak, A. T.; Yatskin, M.; Cheong, P. H.-Y.; Cann, D. P.; Dolgos, M. R. Neutron Total Scattering Studies of Group II Titanates ($ATiO_3$, A^{2+} = Mg, Ca, Sr, Ba). *Sci. Rep.* **2020**, *10* (1), 3729.

(36) de Ligny, D. de; Richet, P. High-Temperature Heat Capacity and Thermal Expansion of $SrTiO_3$ and $SrZrO_3$ Perovskites. *Phys. Rev. B* **1996**, *53* (6), 3013−3022.

(37) Narula, C. K.; Haack, L. P.; Chun, W.; Jen, H.-W.; Graham, G. W. Single-Phase PrO_y-ZrO_2 Materials and Their Oxygen Storage Capacity: A Comparison with Single-Phase CeO_2-ZrO_2, PrO_y-CeO_2, and $PrO_y-CeO_2-ZrO_2$ Materials. *J. Phys. Chem. B* **1999**, *103* (18), 3634−3639.

(38) Hartmann, J. M.; Abbadie, A.; Favier, S. Critical Thickness for Plastic Relaxation of SiGe on Si(001) Revisited. *J. Appl. Phys.* **2011**, *110* (8), No. 083529.

(39) Speck, J. S.; Seifert, A.; Pompe, W.; Ramesh, R. Domain Configurations Due to Multiple Misfit Relaxation Mechanisms in Epitaxial Ferroelectric Thin Films. II. Experimental Verification and Implications. *J. Appl. Phys.* **1994**, *76* (1), 477−483.

(40) Speck, J. S.; Pompe, W. Domain Configurations Due to Multiple Misfit Relaxation Mechanisms in Epitaxial Ferroelectric Thin Films. *I. Theory. J. Appl. Phys.* **1994**, *76* (1), 466−476.

(41) Speck, J. S.; Daykin, A. C.; Seifert, A.; Romanov, A. E.; Pompe, W. Domain Configurations Due to Multiple Misfit Relaxation Mechanisms in Epitaxial Ferroelectric Thin Films. III. Interfacial Defects and Domain Misorientations. *J. Appl. Phys.* **1995**, *78* (3), 1696−1706.

(42) Momma, K.; Izumi, F. VESTA 3 for Three-dimensional Visualization of Crystal, Volumetric and Morphology Data. *J. Appl. Crystallogr.* **2011**, *44* (6), 1272−1276.
(43) Yashima, M.; Hirose, T.; Katano, S.; Suzuki, Y.; Kakihana, M.; Yoshimura, M. Structural Changes of ZrO_2-CeO_2 Solid Solutions around the Monoclinic-Tetragonal Phase Boundary. *Phys. Rev. B* **1995**, *51* (13), 8018−8025.
(44) Yashima, M.; Sasaki, S.; Kakihana, M.; Yamaguchi, Y.; Arashi, H.; Yoshimura, M. Oxygen-Induced Structural Change of the Tetragonal Phase around the Tetragonal−Cubic Phase Boundary in ZrO_2−$YO_{1.5}$ Solid Solutions. *Acta Crystallogr. Sect. B: Struct. Sci.* **1994**, *50* (6), 663−672.
(45) Duwez, P.; Odell, F.; Brown, F. H. Stabilization of Zirconia with Calcia and Magnesia. *J. Am. Ceram. Soc.* **1952**, *35* (5), 107−113.

https://doi.org/10.1021/acsaelm.4c00368
ACS Appl. Electron. Mater. 2024, 6, 5525−5535